



How the fine structure of the electric double layer and the flow affect morphological instability in electrodeposition

I. Rubinstein ^{*} and B. Zaltzman [†]*Blaustein Institutes for Desert Research,**Ben-Gurion University of the Negev, Sede Boqer Campus 8499000, Israel*

(Received 31 July 2022; accepted 10 August 2023; published 7 September 2023)

We analyze the effects of the fine structure of the electric double layer and of the electrode reaction rate upon wavelength selection of the growing perturbation mode in morphological instability in cathodic electrodeposition from a dilute electrolyte solution. The metal cathode is modeled as a cation exchanger with a fixed charge density equal to the average concentration of free electrons that is several orders of magnitude higher than the typical ionic concentration in a solution. This invokes the need to consider the steric modifications in the modeling of the electric double layer at the solution/electrode interface. Accordingly, the results for Bikerman's steric model are compared to those for the classical Nernst-Planck-Poisson-Stokes model valid for pointlike ions. For both models, the diffuse electric double layer splits into a thin inner portion commensurate with the width of the Stern layer and the steric exclusion width, and a much thicker outer portion scaling with the Debye length. For quiescent cathodic electrodeposition, this fine structure combined with a finite electrode reaction rate regularizes the short-wave singularity in morphological instability of the electrodeposition front. This regularization selects a finite range of unstable perturbation modes, with critical wavelength corresponding to the fastest-growing mode. This wavelength scales with the geometric average of the width of the highly charged inner portion of the electric double layer and the reaction-diffusion length, defined as the ratio of cation diffusivity to the electrode reaction rate. The fluid flow induced by the motion of the solid/liquid interface has a negligible effect on morphological instability. At the same time, the emerging electroconvective (electroosmotic) flow in the nonequilibrium regime with its related electroosmotic instability, has a major effect, selecting the width of the cathodic diffusion layer as the dominant length scale for morphological instability and the emerging dendrites. It is observed that the steric correction considerably lowers the voltage threshold for the onset of the nonequilibrium electroosmotic instability.

DOI: [10.1103/PhysRevFluids.8.093701](https://doi.org/10.1103/PhysRevFluids.8.093701)

I. INTRODUCTION

Cathodic electrodeposition of a metal is essential for many industrial applications including electroplating [1–3], synthesis of nanowires as material for electronics and thermoelectric energy applications [4,5], and rechargeable galvanic battery operation [6–10]. Dendrite formation resulting from morphological instability (MI) in electrodeposition and, especially, the role that the related fluid flows play in this process, has been of major interest to physicists in the past three decades [11–16]. This included the study of the effects of electrode kinetics, buoyant, bulk electroconvective, and electroosmotic flows [14,16], the possible role of the bulk electroconvective instability (ECI),

*robinst@bgu.ac.il.

†boris@bgu.ac.il.

and the effects of washing off of the forming dendrites by a tangential flow [16,17]. More recently, Li *et al.* [18,19], addressed the effect of the Butler-Volmer electrode kinetics on ECI in electrodeposition. Since the early 1990s, researchers have discussed the possible role of the extended space charge (ESC) in the dendrite tip formation and flow generation [15,20]. The term ESC pertains to a peculiar charged structure, which forms at a charge-selective interface (electrode, ion exchange membrane, nano-/microchannels' junction) next to the diffuse electric double layer (EDL) under extreme diffusion limitation conditions, when the interface electrolyte concentration approaches zero [21–29]. One kind of MI arising in electrodeposition has recently attracted particular attention of the research community, mainly in the context of the design of galvanic batteries with metal (lithium) electrodes. The problem was that the metallic dendrites that form during battery charging penetrated the porous separators, creating the risk of battery short circuiting and explosion. Thus, controlling dendrite formation presented itself as a major challenge. This issue was tackled in a wide range of studies, including purely theoretical linear stability analyses for the fixed charge model [30], and for the surface conduction/leaky membrane model [31], purely experimental research [6,32,33], and a combined theoretical/experimental study [34].

In our own recent study [35], we addressed the effects of the EDL, electrode kinetics, and electroosmotic flow upon the wavelength selection in MI in cathodic electrodeposition. Without suitable regularization, e.g., by surface tension [36–38], MI is singular in the sense that the infinite wave number perturbation mode grows the fastest. In our study [35], we did not take surface tension into account. This was motivated by two considerations. First, surface energy for a solid/liquid interface is not an easily measurable quantitative parameter. Second, we wished to focus on how the EDL, the finite reaction rate, and, ultimately, the fluid flow may regularize wave number selection. We found that the finite width of the EDL coupled with the finite electrode reaction rate selects the fastest-growing perturbation mode with the wavelength that is the geometric average of the EDL width and the reaction-diffusion length (the ratio of cation diffusivity to the cathodic reaction rate constant). This wavelength is one to two orders of magnitude greater than colloid-size capillary length determined by surface tension. Accordingly, the electroosmotic flow induces a shift toward still longer waves, especially in the nonequilibrium electroosmosis regime related to the formation of the ESC [39]. These findings stand in qualitative agreement with the available experimental observations on dendrite formation in electrodeposition [40,41].

The analysis in Ref. [35] was carried out for unrealistically low fixed charge concentration (FCC) in the cathode, comparable to the average cation concentration in solution. One peculiarity of this regime is the uniform structure of the EDL. This uniformity was observed to yield a negligible effect of the Stern layer upon the wavelength selection. The purpose of this paper is to extend the analysis of Ref. [35] to the realistic range of FCC. If the latter is to be crudely identified with the density of free electrons in the metal, in accord with the Drude model [42,43], it should be many orders of magnitude higher than the typical electrolyte concentration. This invokes the need to take into account the steric modifications to the classical Nernst-Planck-Poisson-Stokes (NPPS) model valid for pointlike ions.

This paper is organized as follows. We begin with a formulation of the cathodic electrodeposition model problem in the classical NPPS formulation. This is followed by the discussion of a suitable steric modification of this model. Next, we recapitulate the basic assumptions underlying the view of a metal cathode as an ion exchanger. This is followed by a straightforward analysis of the EDL for high FCC in both the classical and the sterically modified version. We observe that the EDL unsurprisingly splits into a thin inner sublayer adjacent to the interface in which the Debye length is rescaled by the square root of FCC, and an outer part, scaled by the Debye length. The width of the inner sublayer is commensurate with that of the Stern layer and the steric exclusion length.

Having established this background, we present a linear stability analysis of steady-state electrodeposition incorporating two types of flow. One is the flow induced by the mere propagation of the solid/liquid interface. It is observed that this type of flow, albeit intriguing in principle, has a negligible effect on the course of MI for realistic (low) rates of electrodeposition. The other type of

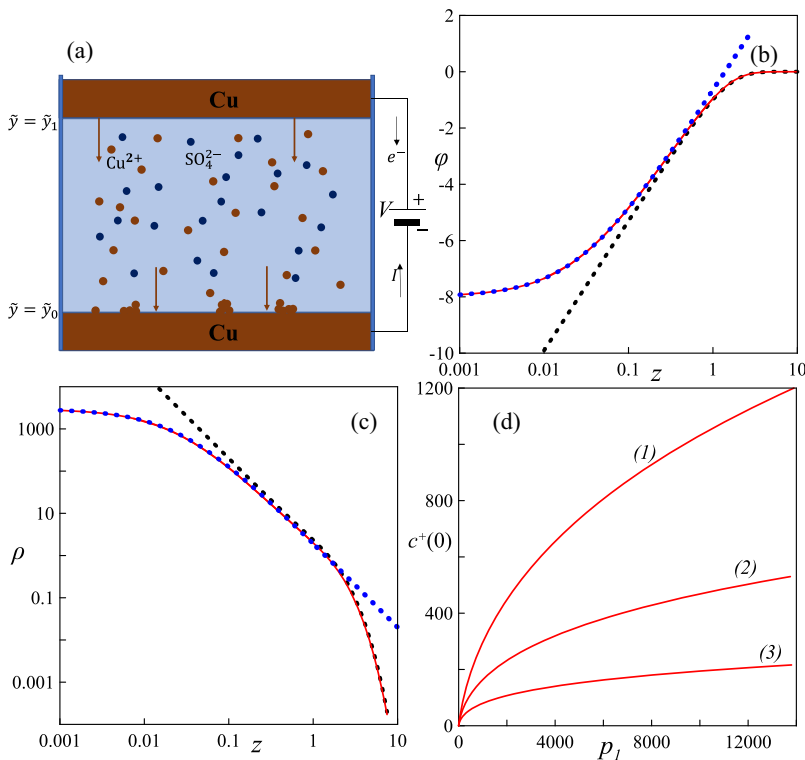


FIG. 1. (a) Scheme of the electrodeposition process and the geometry of the addressed problem; (b) The electric potential $\phi(Z)$ and (c) the charge density ρ vs. scaled distance from the charged wall. $\bar{c}(0) = 1$, $\bar{\varphi}(0) = 0$, $\zeta = -8$ ($A = e^{-4}$). Red continuous lines: exact solutions given by (b) Eq. (18) and (c) Eq. (19b); Blue dotted lines: thin layer approximation, (b) Eq. (20a) and (c) Eq. (20c); Black dotted lines: infinite ζ approximation, (b) Eq. (21a) and (c) Eq. (21c). (d) Cation concentration at the outer edge of the Stern layer, $c^+(0)$, vs. FCC, p_1 , for $\zeta \ll -1$ and (1) $\delta = 0.1$, (2) $\delta = 0.2$, (3) $\delta = 0.4$.

flow is electroosmosis, which has a major effect on electrodeposition in the nonequilibrium regime, just like in the low FCC case [35].

Our linear stability analysis shows that for a realistically high FCC, the Stern layer has a considerable effect on the short-wave features of MI. An unexpected finding is that taking into account the finite ionic size has a major effect upon the onset of the nonequilibrium electroosmotic instability.

II. CATHODIC ELECTRODEPOSITION. MODEL PROBLEM

A. Classical Nernst-Planck-Poisson-Stokes model for pointlike ions.

The two-dimensional boundary value problem for the electrodisolution/deposition process that we address reads as follows. Let the cell be defined as a two-dimensional (2D) layer of a binary electrolyte: $-\infty < \tilde{x} < \infty$, $\tilde{y}_0(\tilde{x}, \tilde{t}) < \tilde{y} < \tilde{y}_1(\tilde{x}, \tilde{t})$. Here, $\tilde{y} = \tilde{y}_0(\tilde{x}, \tilde{t})$ stands for the outer edge of the cathodic Stern layer (Stern layer/solution interface) position of the cathode, whereas $\tilde{y} = \tilde{y}_1(\tilde{x}, \tilde{t})$ stands for its anodic counterpart. Tildes are used to denote dimensional variables, as opposed to their dimensionless counterparts, [see Fig. 1(a) for the geometry]. The classical NPPS model for the ionic transport considers the electrolyte as a dilute solution of the pointlike charges (ions) and reads:

$$\frac{\partial \tilde{c}^\pm}{\partial \tilde{t}} = -\nabla \tilde{\mathbf{J}}^\pm, \quad (1a)$$

$$\tilde{\mathbf{J}}^\pm \stackrel{\text{def}}{=} \tilde{\mathbf{v}}\tilde{c}^\pm - D^\pm \left(\nabla\tilde{c}^\pm + \frac{Fz^\pm\tilde{c}^\pm}{RT} \nabla\tilde{\varphi} \right) \quad (1b)$$

$$d\Delta\tilde{\varphi} = -4\pi\tilde{\rho}, \quad \tilde{\rho} \stackrel{\text{def}}{=} F(z^+\tilde{c}^+ + z^-\tilde{c}^-), \quad (1c)$$

$$m\tilde{\mathbf{v}}_t = -\nabla\tilde{p} - \tilde{\rho}\nabla\tilde{\varphi} + \eta\Delta\tilde{\mathbf{v}}, \quad \nabla \cdot \tilde{\mathbf{v}} = 0. \quad (1d)$$

The Nernst-Planck equations are introduced in (1a), with \tilde{c}^+ and \tilde{c}^- as cationic and anionic concentrations, $\tilde{\mathbf{J}}^+$ and $\tilde{\mathbf{J}}^-$ being the respective fluxes, defined by (1b), where $\tilde{\mathbf{v}} = \tilde{u}\mathbf{i} + \tilde{v}\mathbf{j}$ is the fluid velocity, $\tilde{\varphi}$ the electric potential, D^+ and D^- cationic and anionic diffusivities, and z^+ and z^- are the cationic and anionic charge numbers (in what follows, for brevity, we assume $D^+ = D^- = D$, $z^+ = -z^- = z$). F is the Faraday constant, R is the universal gas constant, and T is the absolute temperature. Equation (1c) is the Poisson equation for the electric potential, where d is the dielectric constant of the solution and $\tilde{\rho}$ is the space charge density due to the local imbalance of ionic concentrations. Finally, (1d) are the Stokes and continuity equations, where m is solution density assumed constant, \tilde{p} is the pressure, η is the dynamic viscosity, and $-\tilde{\rho}\nabla\tilde{\varphi}$ is the electrical volume force acting in the fluid.

The following boundary conditions are imposed on the electrodes. The cathode, $\tilde{y} = \tilde{y}_0(\tilde{x}, \tilde{t})$, is characterized by:

$$\mathbf{n} = -\frac{\tilde{y}_{0\tilde{x}}}{\sqrt{1 + \tilde{y}_{0\tilde{x}}^2}}\mathbf{i} + \frac{1}{\sqrt{1 + \tilde{y}_{0\tilde{x}}^2}}\mathbf{j}, \quad \boldsymbol{\tau} = \frac{1}{\sqrt{1 + \tilde{y}_{0\tilde{x}}^2}}\mathbf{i} + \frac{\tilde{y}_{0\tilde{x}}}{\sqrt{1 + \tilde{y}_{0\tilde{x}}^2}}\mathbf{j}, \quad (2a)$$

$$\tilde{c}_M \frac{\tilde{y}_{0\tilde{t}}}{\sqrt{1 + \tilde{y}_{0\tilde{x}}^2}} = D \left[\nabla\tilde{c}^+ + \frac{Fz\tilde{c}^+}{RT} \nabla\tilde{\varphi} \right] \cdot \mathbf{n}, \quad (2b)$$

$$\tilde{\varphi} - \tilde{\lambda}_S \nabla\tilde{\varphi} \cdot \mathbf{n} = 0, \quad (2c)$$

$$D \left[\nabla\tilde{c}^+ + \frac{Fz\tilde{c}^+}{RT} \nabla\tilde{\varphi} \right] \cdot \mathbf{n} = K_c \tilde{c}^+ \exp\left(\frac{\alpha_c z F}{RT} \tilde{\varphi}\right) - K_a \tilde{c}_M \exp\left(-\frac{\alpha_a z F}{RT} \tilde{\varphi}\right), \quad (2d)$$

$$\left[\nabla\tilde{c}^- - \frac{Fz\tilde{c}^-}{RT} \nabla\tilde{\varphi} \right] \cdot \mathbf{n} = 0, \quad (2e)$$

$$\mathbf{v} \cdot \boldsymbol{\tau} = 0, \quad \mathbf{v} \cdot \mathbf{n} = \frac{\tilde{y}_{0\tilde{t}}}{\sqrt{1 + \tilde{y}_{0\tilde{x}}^2}}. \quad (2f)$$

The free boundary condition (2b) models the propagation of the cathode surface due to electrodeposition. Here, \tilde{c}_M is the constant molar concentration of the electrode metal atoms, whereas the right-hand side is the normal diffusion/migration component of the cationic flux. Boundary condition (2c) prescribes the potential drop across the Stern layer, while postulating zero potential of the cathode. Here, $\tilde{\lambda}_S$ stands for the effective width of the Stern layer [29]. The right-hand side of Eq. (2d) stands for the Butler-Volmer electrode reaction kinetics [29,44,45]. Here, K_c and K_a are rate constants for the cathodic and anodic reactions, dependent on the type of cation, nature of the electrode surface and obeying an Arrhenius-type dependence on temperature, and α_c , α_a are the transfer coefficients for these reactions. We set $\alpha_c = \alpha_a = \frac{1}{2}$, corresponding to single electron transfer reactions [29]. Boundary condition (2e) corresponds to impermeability of the moving cathode's surface for anions. Finally, Eqs. (2f) are the no-slip conditions prescribing the normal component of fluid velocity equal to the speed of the cathode surface propagation in the normal

direction and vanishing tangential component of the fluid velocity at the interface. The anode, $\tilde{y} = l + \tilde{y}_1(\tilde{x}, \tilde{t})$, is described by:

$$\mathbf{n} = \frac{\tilde{y}_{1\tilde{x}}}{\sqrt{1 + \tilde{y}_{1\tilde{x}}^2}} \mathbf{i} + \frac{-1}{\sqrt{1 + \tilde{y}_{1\tilde{x}}^2}} \mathbf{j}, \quad \boldsymbol{\tau} = \frac{1}{\sqrt{1 + \tilde{y}_{1\tilde{x}}^2}} \mathbf{i} + \frac{\tilde{y}_{1\tilde{x}}}{\sqrt{1 + \tilde{y}_{1\tilde{x}}^2}} \mathbf{j}, \quad (3a)$$

$$\tilde{c}_M \frac{\tilde{y}_{1\tilde{t}}}{\sqrt{1 + \tilde{y}_{1\tilde{x}}^2}} = -D \left[\nabla \tilde{c}^+ + \frac{Fz\tilde{c}^+}{RT} \nabla \tilde{\varphi} \right] \cdot \mathbf{n}, \quad (3b)$$

$$\tilde{\varphi} - \tilde{\lambda}_S \nabla \tilde{\varphi} \cdot \mathbf{n} = \tilde{V}, \quad (3c)$$

$$D \left[\nabla \tilde{c}^+ + \frac{Fz\tilde{c}^+}{RT} \nabla \tilde{\varphi} \right] \cdot \mathbf{n} = K_c \tilde{c}^+ \exp \left(\frac{zF[\tilde{\varphi} - \tilde{V}]}{2RT} \right) - K_a \tilde{c}_M \exp \left(-\frac{zF[\tilde{\varphi} - \tilde{V}]}{2RT} \right), \quad (3d)$$

$$\left[\nabla \tilde{c}^- - \frac{Fz\tilde{c}^-}{RT} \nabla \tilde{\varphi} \right] \cdot \mathbf{n} = 0, \quad (3e)$$

$$\mathbf{v} \cdot \boldsymbol{\tau} = 0, \quad \mathbf{v} \cdot \mathbf{n} = -\frac{\tilde{y}_{1\tilde{t}}}{\sqrt{1 + \tilde{y}_{1\tilde{x}}^2}}. \quad (3f)$$

The anodic boundary conditions, Eqs. (3), are similar to Eqs. (2), with \tilde{V} standing for the voltage applied between the two electrodes.

We rewrite the boundary value problem (1)–(3) in a dimensionless form by employing the following natural scaling for the basic variables:

$$x = \frac{\tilde{x}}{l}, \quad y = \frac{\tilde{y}}{l}, \quad t = \frac{\tilde{t}}{t_0}, \quad (4a)$$

$$t_0 = \frac{l^2}{D}, \quad \varphi = \frac{zF\tilde{\varphi}}{RT}, \quad c^\pm = \frac{\tilde{c}^\pm}{c_0}. \quad (4b)$$

Here, l is the initial distance between the electrodes and c_0 is the average concentration of the electrolyte.

$$\mathbf{v} = \frac{\tilde{\mathbf{v}}}{v_0}, \quad v_0 = \frac{d}{4\pi\eta l} \left(\frac{RT}{Fz} \right)^2, \quad p = \frac{\tilde{p}l}{\eta v_0}. \quad (5)$$

The dimensionless governing equations read:

$$\frac{\partial c^+}{\partial t} = -\nabla \mathbf{J}^+, \quad (6a)$$

$$\frac{\partial c^-}{\partial t} = -\nabla \mathbf{J}^-, \quad (6b)$$

$$\mathbf{J}^\pm = \mathbf{v} c^\pm - (\nabla c^\pm \pm c^\pm \nabla \varphi), \quad (6c)$$

$$\varepsilon^2 \Delta \varphi = c^- - c^+, \quad (6d)$$

$$\frac{1}{Sc} \mathbf{v}_t = -\nabla p + \kappa \Delta \varphi \nabla \varphi + \Delta \mathbf{v}, \quad \nabla \cdot \mathbf{v} = 0. \quad (6e)$$

Here, ε is the dimensionless Debye length,

$$\varepsilon = \frac{r_d}{l}, \quad r_d = \sqrt{\frac{dRT}{4z^2\pi c_0 F^2}}, \quad (7)$$

where r_d is the dimensional Debye length. Furthermore, $\kappa, \kappa = \frac{d}{4\pi\eta D} \left(\frac{RT}{Fz} \right)^2$, is the electroconvective coupling coefficient identical to the material Peclet number employed in our previous studies

[46–48]. The advantage of this scaling, previously employed by Demekhin and his colleagues [49,50], is that it leaves the convection term in the ionic flux expression (6c) free of the control parameter, with flow velocity determined by either electroconvection or the propagation of the free boundary. Finally, Sc , $Sc = \frac{t_0 \eta}{ml^2}$, is the Schmidt number. For realistic physical situations $Sc \gg 1$. Thus, in what follows, we set the left-hand side of Eq. (6e) equal to zero.

The dimensionless cathodic boundary conditions, $y = y_0(x, t) = Ut + z_0(x, t)$, read:

$$\rho(U + z_{0t}) = [-(c_x^+ + c^+ \varphi_x)z_{0x} + c_y^+ + c^+ \varphi_y], \quad (8a)$$

$$\frac{1}{\sqrt{1 + z_{0x}^2}} [-(c_x^+ + c^+ \varphi_x)z_{0x} + c_y^+ + c^+ \varphi_y] = k_C(c^+ e^{\frac{\varphi}{2}} - p_1 e^{-\frac{\varphi}{2}}), \quad (8b)$$

$$\varphi - \frac{\lambda}{\sqrt{1 + z_{0x}^2}} (-\varphi_x z_{0x} + \varphi_y) = 0, \quad (8c)$$

$$-(c_x^- - c^- \varphi_x)z_{0x} + c_y^- - c^- \varphi_y = 0, \quad (8d)$$

$$-uz_{0x} + w = U + z_{0t}, \quad u + wz_{0x} = 0. \quad (8e)$$

Here, U is the average velocity of the cathodic surface propagation (velocity of the flat free boundary in mathematical terms), $z_0(x, t)$ is the dimensionless deviation of the cathodic surface from flatness (the perturbation of the flat boundary in the subsequent linear stability analysis).

$$k_C = \frac{K_c l}{D}, \quad k_A = \frac{K_a l}{D} \quad (9)$$

are the dimensionless rate constants for the cathodic and anodic reactions,

$$\rho = \frac{\tilde{c}_M}{c_0}, \quad p_1 = \frac{k_A \tilde{c}_M}{k_C c_0}, \quad \lambda = \frac{\lambda_S}{l}. \quad (10)$$

For the sake of simplicity, we assume an infinitely high reaction rate (reaction equilibrium) and vanishing capacity of the Stern layer on the anode/solution interface, and postulate flatness of the anodic surface. We also neglect the effect of the anodic EDL on the MI and impose the boundary conditions on the outer edge of the anodic EDL. Under these assumptions, the dimensionless anodic boundary conditions, at $y = y_1(x, t) = 1 + Ut$, assume the following form:

$$c_y^- - c^- \varphi_y = 0, \quad c^+ = c^-, \quad \ln c^+ + \varphi = \ln p_1 + V, \quad w = U, \quad u = 0. \quad (11)$$

$V = \frac{zF\tilde{V}}{RT}$ in the right-hand side of the continuity condition for the electrochemical potential is the dimensionless voltage. By transformation to the moving frame, that is, by replacing the variable y by z defined as $z = y - Ut$, and the velocity \mathbf{v} by $\mathbf{v}_1 \stackrel{\text{def}}{=} u_1 \mathbf{i} + w_1 \mathbf{j} = \mathbf{v} - U \mathbf{j}$, the model problem (6), (8), (11) is rewritten as

$$z_0(x, t) < z < 1 : \frac{\partial c^\pm}{\partial t} + \mathbf{v}_1 \nabla c^\pm = \nabla (\nabla c^\pm \pm c^\pm \nabla \varphi), \quad (12a)$$

$$\varepsilon^2 \Delta \varphi = c^- - c^+, \quad (12b)$$

$$0 = -\nabla p + \kappa \Delta \varphi \nabla \varphi + \Delta \mathbf{v}_1, \quad \nabla \cdot \mathbf{v}_1 = 0; \quad (12c)$$

$$\begin{aligned} z = z_0(x, t) : \rho(U + z_{0t}) \\ = [-(c_x^+ + c^+ \varphi_x)z_{0x} + c_z^+ + c^+ \varphi_z], \end{aligned} \quad (12d)$$

$$\frac{1}{\sqrt{1 + z_{0x}^2}} [-(c_x^+ + c^+ \varphi_x)z_{0x} + c_z^+ + c^+ \varphi_z] = k_C(c^+ e^{\frac{\varphi}{2}} - p_1 e^{-\frac{\varphi}{2}}), \quad (12e)$$

$$\varphi - \frac{\lambda}{\sqrt{1+z_{0x}^2}}(-\varphi_x z_{0x} + \varphi_z) = 0, \quad (12f)$$

$$-(c_x^- - c^- \varphi_x) z_{0x} + c_z^- - c^- \varphi_z = 0, \quad (12g)$$

$$-u z_{0x} + w_1 = z_{0t}, \quad u + (w_1 + U) z_{0x} = 0; \quad (12h)$$

$$z = 1 : c_y^- - c^- \varphi_z = 0, \quad c^+ = c^-, \quad \ln c^+ + \varphi = \ln p_1 + V, \quad w_1 = u_1 = 0. \quad (12i)$$

We complete the model description by determining the physically relevant range of the control parameters. For a 10^{-2} M– 10^{-1} M diluted aqueous solution of copper sulfate extensively used in the experiments, e.g., Refs. [12–14,16–20,37], the relevant parameters are as follows: $D = 7 \times 10^{-6} \frac{\text{cm}^2}{\text{s}}$, $z = 2$, $K_a = K_c = 1.34 \times 10^{-5} \frac{\text{cm}}{\text{s}}$, $\eta = 1.8 \times 10^{-2} \frac{\text{g}}{\text{cm}\cdot\text{s}}$, $\tilde{\rho} = 140$ M, $r_d \sim 7 \times 10^{-8}$ – 2.5×10^{-7} cm, $\lambda_S \sim 5 \times 10^{-8}$ – 10^{-7} cm. For $l \sim 10^{-2}$ – 10^{-1} cm-thick electrolyte layer, we find $\rho = p_1 \sim 1.4 \times 10^3$ – 1.4×10^4 , $\varepsilon \sim 7 \times 10^{-7}$ – 2.5×10^{-5} , $\kappa = 0.1$, $k_C = k_A \sim 2 \times 10^{-2}$ – 2×10^{-1} , $\lambda \sim 5 \times 10^{-8}$ – 10^{-6} . In what follows we address this range of the dimensionless physical parameters and assume that $\rho = p_1$.

B. Incorporating the steric effects in the electrodeposition model.

To investigate the possible effect of overcrowding of cations near the cathode, we are going to employ the steric regularizations of the classical Poisson-Boltzmann (PB) EDL model. Historically, the first modified Poisson-Boltzmann (mPB) model, taking into account the effect of the finite ionic size (the ionic steric effect) was due to Bikerman [51]. In this model, the expression for the ionic electrochemical potentials is modified in order to take into account the constraint on the volume available for ions. The recent progress in the studies of ionic liquids and the development of various engineering applications, such as microfluidic devices, microbatteries, and electrochemical sensors, brought about the need to further refine the mPB model. The goal was to improve the description of the response of an electrolyte to a high applied voltage, large enough to cause crowding of ions near the electrode surface with the bulk solution remaining dilute [45,51–63].

The recent steric mPB models [45,59–62], either based on the Landau-Ginzburg-type approach, taking into account the short-range Coulomb correlations, such as the Bazant-Storey-Kornishev (BSK) model [59], or the cluster model by Ram, Adar, and Andelman [63], yield replacing the common Poisson equation for the electric potential by a suitable fourth-order equation. Below we outline the mathematical framework of the Bikerman mPB model of cathodic electrodeposition to be used in this study and comment on the prospects of employing more advanced steric models [59,63].

In its dimensionless form, the Bikerman model boundary value problem [45], reads:

$$z_0(x, t) < z < 1 : \frac{\partial c^\pm}{\partial t} + \mathbf{v}_1 \nabla c^\pm = \nabla(c^\pm \nabla \mu^\pm),$$

$$\mu^\pm = \ln \frac{c^\pm}{1 - v(c^+ + c^-)} \pm \varphi \quad (13a)$$

$$\varepsilon^2 \Delta \varphi = c^- - c^+, \quad (13b)$$

$$0 = -\nabla p + \kappa \Delta \varphi \nabla \varphi + \Delta \mathbf{v}_1, \quad \nabla \cdot \mathbf{v}_1 = 0; \quad (13c)$$

$$z = z_0(x, t) : p_1(U + z_{0t}) = z[-c^+ \mu_x^+ z_{0x} + c^+ \mu_z^+], \quad (13d)$$

$$\frac{1}{\sqrt{1+z_{0x}^2}}[-c^+ \mu_x^+ z_{0x} + c^+ \mu_z^+] = k_C \sqrt{c^+ p_1} (e^{\frac{\mu^+ - \mu_x^+}{2}} - e^{-\frac{\mu^+ - \mu_x^+}{2}}), \quad \mu_s^+ = \ln p_1 \quad (13e)$$

$$\varphi - \frac{\lambda}{\sqrt{1 + z_{0x}^2}}(-\varphi_x z_{0x} + \varphi_z) = 0, \quad (13f)$$

$$-c^- \mu_x^- z_{0x} + c^- \mu_y^- = 0, \quad (13g)$$

$$-u z_{0x} + w_1 = z_{0r}, \quad u + (w_1 + U) z_{0x} = 0; \quad (13h)$$

$$z = 1 : \mu_z^- = 0, \quad c^+ = c^-, \quad \mu^+ = V + \ln p_1, \quad w_1 = u_1 = 0. \quad (13i)$$

Here μ^\pm are the regularized ionic electrochemical potentials, and ν is the dimensionless ionic volume at zero voltage. The reciprocal of ν defines the maximum possible dimensionless total ionic concentration. In what follows we consider $\nu \sim 10^{-3}$ – 10^{-1} , corresponding to the 0.1–10 M range of the maximal total ionic concentration. We note that the Bikerman model (13) is a straightforward generalization of the classical model (12). This latter constitutes a regular asymptotic limit of the Bikerman model for vanishing ionic volume, $\nu = 0$. On the other hand, in the framework of the BSK or Ram-Adar-Andelman model [59], one deals with a singularly perturbed Poisson equation in the form of the following fourth-order equation for the electric potential:

$$\varepsilon^2(1 - \delta^2 \nabla^2) \nabla^2 \varphi = c^- - c^+. \quad (14)$$

Here $\delta = \frac{l_c}{l}$, where l_c is the ionic correlation length which varies from the typical ionic diameter $1\text{--}3 \times 10^{-8}$ cm for high ionic concentrations to the Bjerrum length, $l_B \sim 7 \times 10^{-8}$ cm for dilute electrolytes.

Accordingly, this singularly perturbed Poisson equation has to be complemented by the following additional boundary condition accounting for the vanishing normal derivative of the mean-field charge density at the interface:

$$\mathbf{n} \cdot \nabla(\nabla^2 \varphi) = 0. \quad (15)$$

Due to the extreme complexity of computational implementation of the related generalization for the cathodic electrodeposition problem for realistic range of control parameters, we defer its analysis to a future study and remains in the framework of the classical model and its Bikerman modification.

III. METAL CATHODE AS AN ION EXCHANGER AND THE FINE STRUCTURE OF THE EDL

In the spirit of the Drude model [42,43], we regard the metal cathode as an ion exchanger in which the free electrons play the role of fixed charges. A more precise analogy would be the so-called liquid ion exchanger in which the ion-exchange groups are free to move and redistribute in space. However, here, for simplicity we assume that the interface concentration of free electrons is equal to their average concentration in the metal, assumed to be fixed and independent of the electrode potential. In addition, we assume local electroneutrality in the metal, that is, equality of the metal cation concentration and the free electron concentration, FCC. The cations of the solution are assumed to exchange with those in the metal by means of electrode reaction governed by the Butler-Volmer kinetics. Thus, for a metal electrode with FCC of 10–400 M and a dilute electrolyte with bulk concentration of 1–100 mM, the interface concentration of counterions (assumed to be close to FCC) is expected to be three to five orders of magnitude higher than their bulk concentration, in particular, possibly considerably higher than the limit prescribed by steric restriction. This determines the peculiarity of a quasiequilibrium EDL, which we discuss below.

Motivated by the subsequent applications to MI, below we trace the fine structure of the cathodic EDL for large values of ζ potential in the classical and Bikerman models. Let us start with the classical Gouy-Chapman theory for pointlike ions. According to this theory, the electric potential and the ionic concentrations in the EDL are solutions of the Poisson-Boltzmann equation controlled

by two parameters: ionic concentration (taken in the bulk or on the interface) and the potential drop across the EDL:

$$0 < Z < \infty : \frac{d^2\varphi}{dZ^2} = c^-(Z) - c^+(Z), \quad (16a)$$

$$c^+(Z) = \bar{c}(0)e^{\bar{\varphi}(0)-\varphi(Z)}, \quad (16b)$$

$$c^-(Z) = \bar{c}(0)e^{-\bar{\varphi}(0)+\varphi(Z)}. \quad (16c)$$

Here, $Z = \frac{\zeta-z_0}{\varepsilon}$ is the EDL boundary-layer variable and $\bar{c}(0)$, $\bar{\varphi}(0)$ are, respectively, the electrolyte concentration and the electric potential at the outer edge of the EDL. Integration of Eqs. (16) yields

$$\varphi(Z) = \bar{\varphi}(0) + 2 \ln \frac{e^{\frac{\zeta}{2}} + 1 - (1 - e^{\frac{\zeta}{2}})e^{-Z\sqrt{2\bar{c}(0)}}}{e^{\frac{\zeta}{2}} + 1 + (1 - e^{\frac{\zeta}{2}})e^{-Z\sqrt{2\bar{c}(0)}}}, \quad (17)$$

where $\zeta = \varphi(0) - \bar{\varphi}(0) < 0$, is the potential drop across the diffuse EDL. To characterize the near-the-interface portion of the EDL responsible for the bulk of the cationic concentration variation, let us define the parameter A as $A = e^{\frac{\zeta}{2}} = \sqrt{\frac{\bar{c}(0)}{c^+(0)}}$. Neglecting the transcendently small terms in (17), we obtain the following expression for the electric potential φ in the EDL, which is uniformly valid for large negative ζ and high cationic surface concentration $c^+(0)$:

$$\varphi(Z) = \bar{\varphi}(0) + 2 \ln \frac{2A + 1 - e^{-Z\sqrt{2\bar{c}(0)}}}{1 + e^{-Z\sqrt{2\bar{c}(0)}}}, \quad (18)$$

Differentiation of Eq. (18) yields, upon disregarding the transcendently small terms, the following expressions for the electric field, $E = -\frac{1}{\varepsilon}\varphi'(Z)$, and the electric charge density, $\rho = c^+(Z) - c^-(Z)$:

$$E = -\frac{4\sqrt{2\bar{c}(0)}}{\varepsilon} \frac{e^{-Z\sqrt{2\bar{c}(0)}}}{4A + 1 - e^{-2Z\sqrt{2\bar{c}(0)}}}, \quad (19a)$$

$$\rho = 8\bar{c}(0)e^{-Z\sqrt{2\bar{c}(0)}} \frac{1 + e^{-2Z\sqrt{2\bar{c}(0)}}}{(4A + 1 - e^{-2Z\sqrt{2\bar{c}(0)}})^2}. \quad (19b)$$

For the vicinity of the charged surface, $0 \leq Z\sqrt{\bar{c}(0)} \ll 1$, the following asymptotic approximations hold for the electric potential, the electric field, and the charge density:

$$\varphi(Z) = \varphi(0) + 2 \ln \frac{2 + Z\sqrt{2c^+(0)}}{2}, \quad (20a)$$

$$\varepsilon E = -\frac{2\sqrt{2c^+(0)}}{2 + Z\sqrt{2c^+(0)}}, \quad (20b)$$

$$\rho = \frac{4c^+(0)}{(2 + Z\sqrt{2c^+(0)})^2}. \quad (20c)$$

When the distance from the charged solid exceeds $O(A)$, $O(A) < Z < \infty$, the structure of the EDL is described by the following asymptotic expressions:

$$\varphi(Z) = \bar{\varphi}(0) + 2 \ln \frac{1 - e^{-Z\sqrt{2\bar{c}(0)}}}{1 + e^{-Z\sqrt{2\bar{c}(0)}}}, \quad (21a)$$

$$\varepsilon E = -4\sqrt{2\bar{c}(0)} \frac{e^{-Z\sqrt{2\bar{c}(0)}}}{1 - e^{-2Z\sqrt{2\bar{c}(0)}}}, \quad (21b)$$

$$\rho = 8\bar{c}(0)e^{-Z\sqrt{2\bar{c}(0)}} \frac{1 + e^{-2Z\sqrt{2\bar{c}(0)}}}{(1 - e^{-2Z\sqrt{2\bar{c}(0)}})^2}. \quad (21c)$$

Thus, for large ζ and $c^+(0) \gg 1$, the EDL splits into two parts: a thin, $O(\frac{\varepsilon}{\sqrt{c^+(0)}})$ -wide compact sublayer adjacent to the charged wall in which the electric field and the charge density are functions of the cationic wall concentration $[c^+(0)]$ and where the major part of the EDL charge is located, and a much wider, $O(\frac{\varepsilon}{\sqrt{\bar{c}(0)}})$ -wide residual sublayer, the tail, where these characteristics are solely determined by the bulk concentration, $\bar{c}(0)$. These asymptotic expressions, (21), are valid for the tail, $Z \gg A$, and are singular at $Z = 0$, corresponding to an infinite ζ potential [46]. Equations (20), (21) describe the fine structure of the EDL in the vicinity of the wall in terms of the dependence of the electric field and the electric charge density on ζ and the wall concentration $c^+(0)$. In Figs. 1(b)–1(c) we illustrate this structure by plotting the electric potential, the electric field and charge density profiles for a sequence of A .

To evaluate the effect of the Stern layer on ionic overcrowding we refer to zero electric potential being zero at the cathode and complement the EDL model, (16), by the following 1D version of Eq. (13f):

$$\varphi(0) = \delta \frac{d\varphi}{dZ}, \quad (22)$$

where $\delta = \frac{\lambda}{\varepsilon}$. Then, for the equilibrium EDL (zero electric current) and high ζ potential, $\zeta \ll -1$, we find, keeping the leading-order terms in Eq. (17):

$$p_1 = c^+(0)e^{\delta\sqrt{\frac{c^+(0)}{2}}}. \quad (23)$$

For $p_1 \gg 1$, this yields

$$c^+(0) \approx 2 \left(\frac{\ln p_1}{\delta} \right)^2. \quad (24)$$

Therefore, as shown in Fig. 1(d), even for high FCC of the order of 10^2 M, for a realistic width of the Stern layer the ionic concentration at its outer edge does not exceed 10 M.

To account for the steric effect in overcrowding of cations near the cathode for large negative ζ , we employ the Bikerman regularization of the PB EDL model (13) and rewrite it in terms of the inner EDL variable Z :

$$0 < Z < \infty : \frac{d^2\varphi}{dZ^2} = c^-(Z) - c^+(Z), \quad (25a)$$

$$\frac{d\mu^\pm}{dZ} = 0, \quad (25b)$$

$$c^\pm = \frac{e^{\mu^\pm \mp \varphi}}{1 + \nu(e^{\mu^+ - \varphi} + e^{\mu^- + \varphi})}. \quad (25c)$$

Integrating Eq. (25b) and substituting the boundary conditions at the outer edge of the EDL, we find

$$\mu^+ - \bar{\varphi}(0) = \mu^- + \bar{\varphi}(0) = \ln \frac{\bar{c}(0)}{1 - 2\nu\bar{c}(0)}, \quad (26)$$

and rewrite Eq. (25a) as follows:

$$\frac{d^2\varphi}{dZ^2} = \bar{c}(0) \frac{e^{\varphi - \bar{\varphi}(0)} - e^{-\varphi + \bar{\varphi}(0)}}{1 + \nu\bar{c}(0)(e^{\varphi - \bar{\varphi}(0)} + e^{-\varphi + \bar{\varphi}(0)} - 2)}, \quad (27)$$

Next multiplying Eq. (27) by $\varphi'(Z)$ and integrating the obtained equality we obtain:

$$\sqrt{\nu} \frac{d\varphi}{dZ} = \sqrt{2 \ln[1 + \nu\bar{c}(0)(e^{\frac{\bar{\varphi}(0) - \varphi}{2}} - e^{-\frac{\varphi - \bar{\varphi}(0)}{2}})^2]}. \quad (28)$$

Therefore, for the moderate values of ζ potential, $\nu\bar{c}(0)e^{\frac{\zeta}{2}} \ll 1$, the steric effect is negligible and its solution up to the leading order is given by Eq. (17). For the large negative values of ζ potential,

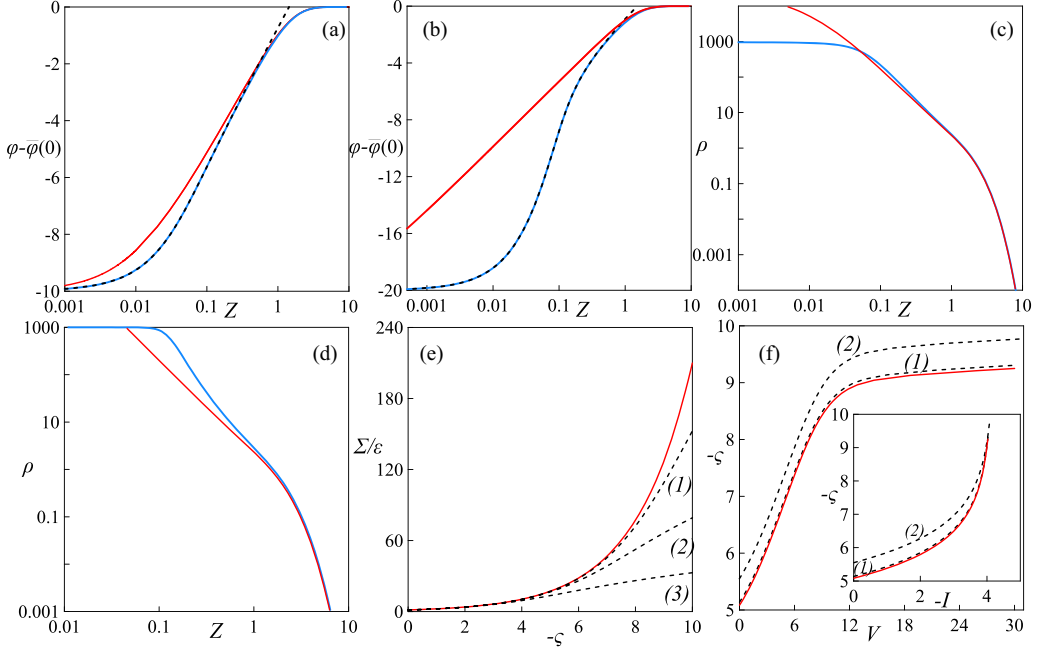


FIG. 2. (a), (b) The drop of the electric potential $\varphi(Z) - \bar{\varphi}(0)$ vs. scaled distance from the charged wall for $\bar{c}(0) = 1$, $\nu = 0.001$, and $\zeta = -10$ (a), $\zeta = -20$ (b). Blue continuous line: solution to Eqs. (25). Red continuous line: solution to the classical model (17). Black dashed lines: thin layer approximation, Eq. (29). (c), (d) The charge density $\rho = c^+ - c^-$ vs. scaled distance from the charged wall for $\bar{c}(0) = 1$, $\nu = 10^{-3}$ and $\zeta = -10$ (c), $\zeta = -20$ (d). Blue line: solution to Eqs. (25). Red line: solution to the PB model (17). (e) The dependence of the EDL total charge Σ on ζ -potential for $\bar{c}(0) = 1$. Red continuous line: PB model, $\nu = 0$; Black dashed lines: solution to the mPB model, Eqs. (25), for (1) the intermediate steric effect, $\nu = 10^{-3}$, (2) the severe steric effect, $\nu = 10^{-2}$, (3) the extreme steric effect, $\nu = 10^{-1}$. (f) ζ potential, ζ , vs. dimensionless voltage V computed by solving the 1D steady-state version of Eqs. (12) and (13). Red continuous line: vanishing steric parameter, $\nu = 0$, Eqs. (12); black dashed line: steric effect model, Eq. (13); $\nu = 10^{-3}$ (1), $\nu = 10^{-2}$ (2). Inset: Same plots for the dependence of ζ on the dimensionless electric current J . $p_1 = 14000$, $\varepsilon = 2 \times 10^{-5}$, $\lambda = 5 \times 10^{-6}$, $k_C = 2 \times 10^{-2}$.

$\nu \bar{c}(0) e^{\frac{\zeta}{2}} \geq O(1)$, the EDL splits into two parts, as in the PB model. The first $O(\varepsilon)$ -wide part is the tail, where these characteristics are solely determined by the bulk concentration, $\bar{c}(0)$, and are described by Eq. (21). To describe the thin compact component of the EDL adjacent to the charged wall we consider the region of high potential drop, $\varphi(Z) - \bar{\varphi}(0) \gg 1$, and disregarding the transcendently small terms in Eq. (28), we obtain the following simplified equation:

$$\frac{dY}{Y \sqrt{2(1+Y)}} = -\frac{dZ}{\sqrt{\nu}}, \quad (29)$$

where $Y = \nu \bar{c}(0) e^{\bar{\varphi}(0) - \varphi(Z)}$.

Thus, accounting for the steric effect yields the $O(\sqrt{\nu \varepsilon})$ width of the compact, strongly charged portion of the EDL adjacent to the cathode surface instead of $O(\frac{\varepsilon}{\sqrt{c^+(0)}})$ derived above within the PB model.

In Fig. 2, we illustrate the EDL characteristics for the 1D steady state in the PB, Eqs. (12), and mPB, Eqs. (13), models for the set of control parameters corresponding to a 10^{-2} M solution of the copper sulphate. In Figs. 2(a), 2(b) we observe the emergence of the new $\sqrt{\nu \varepsilon}$ EDL length scale for the high ζ -potential regime in the steric model (the dashed line vs. the continuous blue line). The

actual dimensionless width of the compact highly charged EDL sublayer adjacent to the cathode is about $10\sqrt{\nu\varepsilon}$ and slightly increases with the increase of ζ potential. For high voltage (close to or above the limiting current, $I = -c^+\mu_z^+ = -4$), the concentration at the outer edge of the EDL approaches zero and the ESC forms. Simultaneously, the total ionic concentration constraint $\frac{1}{\nu}$ yields saturation of the interface charge density, implying its decrease in comparison to the classical model, Eqs. (16), and increase at the outer edge of the compact sublayer, Figs. 2(c), 2(d). Subsequently, we will see that this charge redistribution has a substantial effect on the onset of the nonequilibrium electroosmotic vortical flow and, thus, affects the wavelength selection in MI. To complete this outline of the EDL structure in the steric model (25), we present the dependence of the total EDL charge, $\Sigma = \varepsilon \frac{d\varphi}{dz}(0)$, on ζ potential, Fig. 2(e), and of ζ potential on voltage, Fig. 2(f), and current density I , inset to Fig. 2(f), for the varying steric constraint parameter ν .

IV. EFFECTS OF THE FINE STRUCTURE OF THE ELECTRIC DOUBLE LAYER AND OF THE FLOW ON THE MODE SELECTION IN MORPHOLOGICAL INSTABILITY

In this section we study MI of the quiescent, 1D steady-state solution to the problem (13), which reads: $c^+(x, z, t) = c_0^+(z)$, $c^-(x, z, t) = c_0^-(z)$, $\varphi(x, z, t) = \varphi_0(z)$, $\mathbf{v}_1 = 0$, $z_0(x, t) = 0$, $z_1(x, t) = 0$.

$$0 < z < 1 : c_0^+ \mu_0^{+'} = p_1 U = J, \quad \mu_0^+ = \ln \frac{c_0^+}{1 - \nu(c_0^+ + c_0^-)} + \varphi_0; \quad (30a)$$

$$c_0^- \mu_0^{-'} = 0, \quad \mu_0^- = \ln \frac{c_0^-}{1 - \nu(c_0^+ + c_0^-)} - \varphi_0; \quad (30b)$$

$$\varepsilon^2 \varphi_0'' = c_0^- - c_0^+, \quad (30c)$$

$$z = 0 : p_1 U = k_C \sqrt{c_0^+} (e^{\frac{\mu_0^+}{2}} - p_1 e^{-\frac{\mu_0^+}{2}}), \quad \varphi_0 - \lambda \varphi_0' = 0, \quad (30d)$$

$$z = 1 : c_0^+ = c_0^-, \quad \ln c_0^+ + \varphi_0 = \ln p_1 + V, \quad (30e)$$

$$\int_0^1 c_0^-(z) dz = 1. \quad (30f)$$

Here, J in Eq. (30a) is the absolute value of the dimensionless electric current. Equation (30f) prescribes the total mass of anions in the diffusion layer. We carry out a linear stability analysis of this solution with a focus on the following three cases: (i) classical model for pointlike ions, $\nu = 0$; (ii) intermediate steric restriction, $\nu = 10^{-3}$, (in dimensional terms, this corresponds to an approximately 10 Molar maximum total ionic concentration for a ten-millimolar bulk solution); (iii) severe steric restriction, $\nu = 10^{-2}$ (1 Molar maximum total ionic concentration for a ten-millimolar bulk solution).

We begin with $\kappa = 0$, corresponding to a vanishing electroconvective effect of MI and address the following simplified formulation in which we omit the electrical force term in the Stokes equation (13c):

$$0 = -\nabla p + \Delta \mathbf{v}_1, \quad \nabla \cdot \mathbf{v}_1 = 0. \quad (31)$$

Let us consider a perturbation of the solution (30) of the form:

$$c^\pm = c_0^\pm(z) + \alpha C^\pm(x, z, t), \quad \mu^\pm = \mu_0^\pm + \alpha M^\pm(x, z, t), \quad (32a)$$

$$\varphi = \varphi_0(z) + \alpha \Phi(x, z, t), \quad w_1 = \alpha W(z, x, t), \quad z_0 = \alpha Z(x, t). \quad (32b)$$

Here, $\alpha \ll 1$ is the perturbation parameter. Linearization with respect to α followed by the Fourier and Laplace transforms,

$$C^\pm(x, z, t) = C^\pm(z) e^{ikx} e^{St}, \quad M^\pm(x, z, t) = M^\pm(z) e^{ikx} e^{St}, \quad (33a)$$

$$\Phi(x, z, t) = \Phi(z) e^{ikx} e^{St}, \quad W(z, x, t) = W(z) e^{ikx} e^{St}, \quad Z(x, t) = e^{ikx} e^{St}, \quad (33b)$$

yield the following linear stability problem:

$$0 < z < 1 : SC^+ + Wc_0^{+'} = (c_0^+M^{+'})' - k^2c_0^+M^+ + J\left(\frac{C^+}{c_0^+}\right)', \quad (34a)$$

$$SC^- + Wc_0^{-'} = (c_0^-M^{-'})' - k^2c_0^+M^-, \quad (34b)$$

$$C^\pm = c_0^\pm(M^\pm \mp \Phi) - \nu c_0^\pm(c_0^+(M^+ - \Phi) + c_0^-(M^- + \Phi)) \quad (34c)$$

$$\varepsilon^2(\Phi'' - k^2\Phi) = C^- - C^+, \quad (34d)$$

$$W^{IV} - 2k^2W'' + k^4W = 0; \quad (34e)$$

$$z = 0 : Sp_1 = c_0^+M^{+'} + C^+\mu_0^{+'}, \quad (34f)$$

$$M^{-'} = 0, \quad (34g)$$

$$c_0^+M^{+'} + C^+\mu_0^{+'} = \frac{J}{2} \frac{C^+ + c_0^{+'}}{c_0^+} + k_C \sqrt{c_0^+} \frac{M^+ + \mu_0^{+'}}{2} (e^{\frac{\mu_0^+}{2}} + p_1 e^{-\frac{\mu_0^+}{2}}), \quad (34h)$$

$$\varphi_0' + \Phi = \lambda(\varphi_0'' + \Phi'), \quad (34i)$$

$$W = S, \quad W' + Uk^2 = 0; \quad (34j)$$

$$z = 1 : C^+ = C^-, \quad M^{-'} = 0, \quad M^+ = 0, \quad W = 0, \quad W' = 0. \quad (34k)$$

First, we address the short-wave perturbations, $k \gg 1$. Introducing the scaled variable $\bar{z} = kz$ and keeping the leading order terms in problem (34), we arrive at the following linear stability problem asymptotically valid in the limit $k \rightarrow \infty$:

$$0 < \bar{z} < \infty : 0 = \frac{d^2M^+}{d\bar{z}^2} - M^+, \quad (35a)$$

$$0 = \frac{d^2M^-}{d\bar{z}^2} - M^-, \quad (35b)$$

$$\frac{d^2\Phi}{d\bar{z}^2} - \Phi = 0, \quad (35c)$$

$$\frac{d^4W}{d\bar{z}^4} - 2\frac{d^2W}{d\bar{z}^2} + W = 0; \quad (35d)$$

$$\bar{z} = 0 : \frac{dM^+}{d\bar{z}} = \frac{dM^-}{d\bar{z}} = \frac{d\Phi}{d\bar{z}} = W - S = \frac{dW}{d\bar{z}} + Uk = 0, \quad (35e)$$

$$Sp_1 = \frac{J}{2} \frac{C^+ + c_0^{+'}}{c_0^+} + k_C \sqrt{c_0^+} \frac{M^+ + \mu_0^{+'}}{2} (e^{\frac{\mu_0^+}{2}} + p_1 e^{-\frac{\mu_0^+}{2}}), \quad (35f)$$

$$\bar{z} = \infty : \frac{dM^+}{d\bar{z}} = \frac{dM^-}{d\bar{z}} = \frac{d\Phi}{d\bar{z}} = \frac{dW}{d\bar{z}} = \frac{d^3W}{d\bar{z}^3} = 0. \quad (35g)$$

Straightforward solution of problem (35) yields: $M^+ = M^- = C^+ = C^- = \Phi = 0$, $W = Se^{-\bar{z}} + (-Uk + S)\bar{z}e^{-\bar{z}}$. Applying Eq. (35) we obtain:

$$S \approx \frac{J}{p_1 \sqrt{1 - \nu c_0^+(0)}} \left(k_C e^{\frac{\varphi_0(0)}{2}} - \frac{\varphi_0(0)}{2\lambda} (1 - \nu c_0^+(0))^{\frac{3}{2}} \right). \quad (36)$$

We note that the asymptotic growth rate, S , is finite and negative for the realistic values of ζ potential. For a very large negative ζ such that the interface cation concentration is very close to

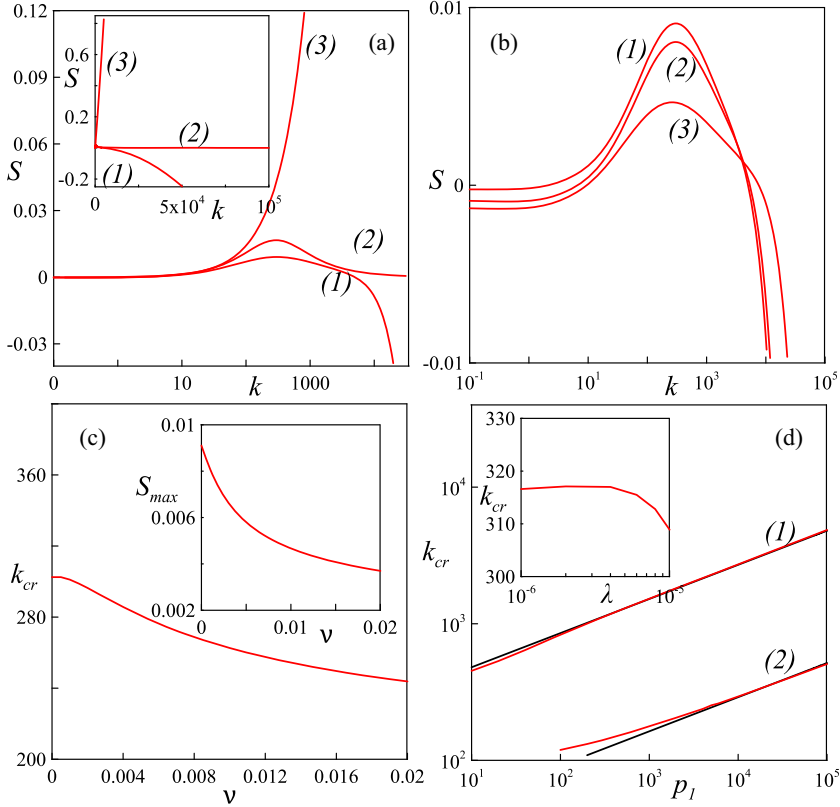


FIG. 3. (a) Growth rate S vs. wave number k ; $p_1 = 1.4 \times 10^4$, $J = 2$ ($V = 2.2$), $\varepsilon = 2 \cdot 10^{-5}$, $\nu = 0$; (1) $k_C = 0.02$, $\lambda = 2 \times 10^{-6}$; (2) $k_C = 0.02$, $\lambda = 0$; (3) $k_C = \infty$, $\lambda = 0$. Inset: same plots in linear scale. (b) Growth rate S vs. wave number k ; $p_1 = 1.4 \times 10^4$, $J = 2$ ($V = 2.2$), $\varepsilon = 2 \times 10^{-5}$, $k_C = 0.02$, $\lambda = 2 \times 10^{-6}$; (1) classical pointlike-ions model $\nu = 0$; (2) intermediate steric effect, $\nu = 0.001$, corresponding to a 10 Molar maximum total ionic concentration for a ten-millimolar bulk solution; (3) severe steric effect, $\nu = 0.01$, corresponding to a Molar maximum total ionic concentration for a ten-millimolar bulk solution. (c) Critical wave number k_{cr} vs. steric parameter ν ; the remaining parameters are the same as for plot (a), curve (1). Inset: Maximal growth rate S_{max} vs. ν . (d) Critical wave number k_{cr} vs. p_1 for $J = 2$ and (1) $k_C = 0.02$, $\varepsilon = 2 \times 10^{-6}$, $\lambda = 2 \times 10^{-7}$, (2) $k_C = 0.02$, $\varepsilon = 2 \cdot 10^{-5}$, $\lambda = 2 \times 10^{-6}$. Black lines— power law approximations $k_{cr} = 270p_1^{1/4}$ (1) and $k_{cr} = 29p_1^{1/4}$ (2). Inset: k_{cr} vs. λ for $p_1 = 1.4 \times 10^4$; the remaining parameters are the same as for curve (2).

its maximum:

$$1 > \nu c_0^+(0) > 1 - (\lambda k_C)^{\frac{2}{3}}, \quad (37)$$

the asymptotic value of S becomes positive.

In the limit of the infinite reaction rate, $k_C = \infty$, $S = O(k) = sk$, Eqs. (34f)–(34j) yield:

$$\bar{z} = 0 : c_0^+ \frac{dM^{+'}}{d\bar{z}} - p_1 s = 0, \quad \frac{dM^{+'}}{d\bar{z}} = 0, \quad \frac{d\Phi}{d\bar{z}} = 0, \quad (38a)$$

$$M^+ + \frac{d\mu_0^{+'}}{d\bar{z}} = 0, \quad (38b)$$

$$W - sk = \frac{dW}{d\bar{z}} + Uk = 0. \quad (38c)$$

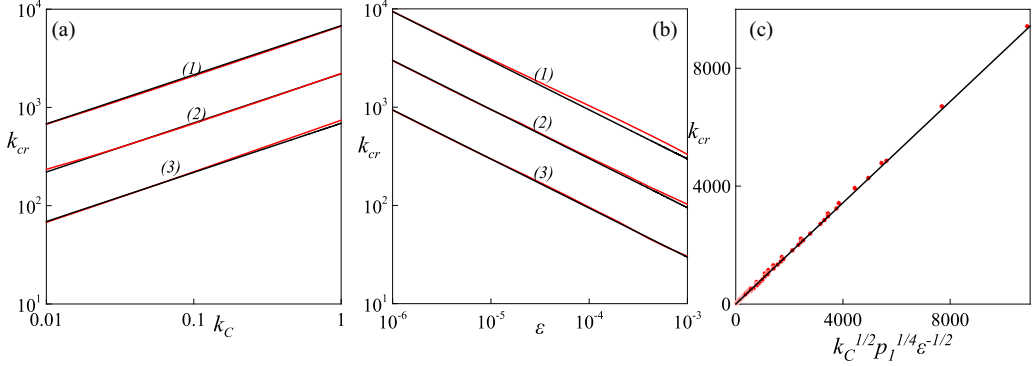


FIG. 4. (a) Red lines: critical wave number k_{cr} vs. reaction rate k_C , $p_1 = 1.4 \times 10^4$, $J = 2$ ($V = 2.2$), $\nu = 0$, $\lambda = 10^{-1} \times \varepsilon$, (1) $\varepsilon = 2 \times 10^{-4}$, corresponding to a 10- μm wide diffusion layer in dimensional units. Black line: power-law approximations $k_{cr} = 6800k_C^{1/2}$. (2) $\varepsilon = 2 \times 10^{-5}$, corresponding to a 100- μm wide diffusion layer. Black line: $-k_{cr} = 2200k_C^{1/2}$. (3) $\varepsilon = 2 \times 10^{-6}$, corresponding to a 1 mm wide diffusion layer. Black line: $-k_{cr} = 690k_C^{1/2}$. (b) Red lines: Critical wave number k_{cr} vs. dimensionless Debye length, ε , (1) $k_C = 1$, black line: power law approximations $k_{cr} = 9.4\varepsilon^{-1/2}$; (2) $k_C = 0.1$, black line: $-k_{cr} = 3\varepsilon^{-1/2}$; (3) $k_C = 0.01$, black line: $-k_{cr} = 0.94\varepsilon^{-1/2}$. The remaining parameters are the same as for plot (a). (c) Critical wave number k_{cr} vs. $\sqrt{\frac{k_C \sqrt{p_1}}{\varepsilon}}$, $J = 2$, ($V = 2.2$). Red dots: – computed values of k_{cr} taken from Figs. 3(c), 4(a), 4(b); black line: linear approximation $k_{cr} = \sqrt{\frac{k_C \sqrt{p_1}}{2\varepsilon}}$.

Solving Eqs. (35a)–(35d), (35g), (38) we find that

$$M^- = \Phi = M^+ + \frac{J}{c_0^+(0)} e^{-\bar{z}} = 0, \quad W = s k e^{-\bar{z}} + (s - U) k \bar{z} e^{-\bar{z}}. \quad (39)$$

Substituting Eq. (39) into Eq. (38a) we obtain $s = -\frac{J}{p_1} = U > 0$, implying the return of the short-wave singularity typical of unregularized MI.

In the limit of vanishing width of the Stern layer, $\lambda = 0$, for a finite reaction rate, k_C the short-wave ($k \gg 1$) asymptotic solution to problem (34) reads

$$\Phi = -\varphi'_0(0) e^{-\bar{z}}, \quad M^+ = M^- = 0, \quad W = S e^{-\bar{z}} + (S - U k) \bar{z} e^{-\bar{z}}, \quad (40)$$

and, thus,

$$S \approx \frac{J}{2} \left(J \nu c_0^+(0) + \frac{2k_C}{\sqrt{1 - \nu c_0^+(0)}} \right) > 0. \quad (41)$$

This implies a finite positive nonsingular growth rate in the short-wave limit.

Summarizing, for a finite reaction rate k_C , taking into account the fine structure of the EDL that includes a Stern layer of finite width regularizes the short-wave singularity in MI and yields a finite, albeit large, range of wave numbers for growing perturbation modes. This is illustrated in Fig. 3(a), where the dependence of the growth rate parameter S on the wave number k is presented for the solution to the full problem, (34), and for two asymptotic limits, those of the vanishing width of the Stern layer and of the infinite reaction rate k_C . We show that, for a finite k_C , accounting for the finite width of the Stern layer eliminates the short-wave singularity and defines a finite range of unstable modes. We define the critical wave number $k_{cr} > 0$ as that of the fastest growing mode with $S_{\max} = \max_k S(k) = S(k_{cr})$. For the vanishing electroconvective flow case, $\kappa = 0$, the increase of the steric restriction parameter, $\nu > 0$, mainly affects the maximal growth rate S_{\max} and slightly

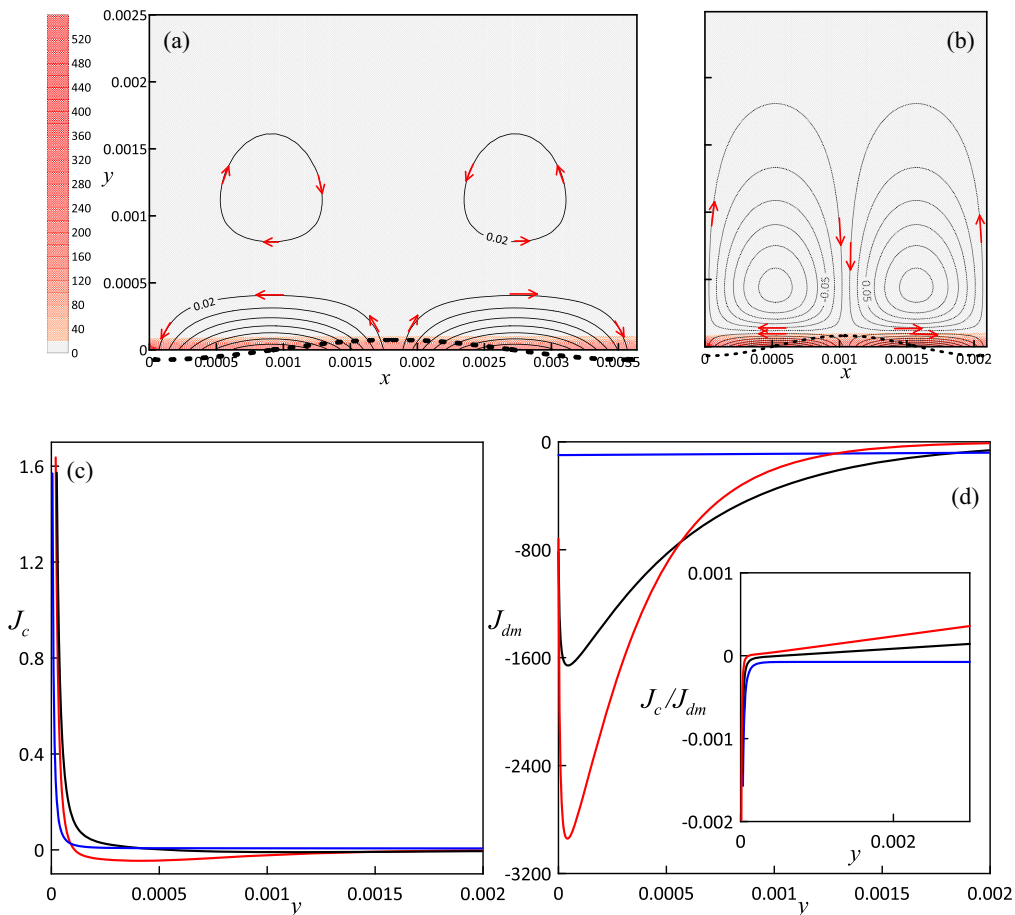


FIG. 5. (a), (b) The flow streamlines for $p_1 = 10^3$, $\varepsilon = 10^{-4}$, $\lambda = 2 \times 10^{-6}$, $k_C = 10$ and $k = k_{cr} = 1727$ (a) and $k = 3000 > k_{cr}$ (b). The dashed black line at the bottom marks the periodic electrode surface distortion. The color scale depicts concentration variation: the red color corresponds to the high values of dimensionless concentration near the electrode surface and the gray color to the relatively low concentration in the tail of the EDL. (c), (d) The dependencies of the convective flux (c) and the diffusion/migration flux (d) components on the dimensionless distance from the electrode surface for $k = 100 < k_{cr}$ (red line), $k = k_{cr} = 1727$ (black line), and $k = 3000 > k_{cr}$ (blue line). Inset to (d): The ratio of the convective and diffusion flux components versus y for the same values of the wave number, k .

reduces the value of the critical wave number, k_{cr} , Figs. 3(a), 3(b). Therefore, in the remainder of our analysis of the ($\kappa = 0$) regime we consider the classical model for pointlike ions, $\nu = 0$. Next, we address the dependence of the critical wavelength, k_{cr} , on the main dimensionless control parameters: the width of the Stern layer, λ , the reaction rate, k_C , the interface cation concentration, p_1 , and the dimensionless Debye length, ε . Whereas a nonvanishing λ is necessary for having a finite range of the instability modes, the critical wave number k_{cr} is barely sensitive to its magnitude [see inset to Fig. 3(d)]. In Fig. 3(d) we also show that k_{cr} is an increasing function of the interface concentration p_1 , that obeys the power law $k_{cr} \sim p_1^{1/4}$ for realistic p_1 .

This complements our earlier observation, Ref. [1], that k_{cr} is an increasing function of k_C , obeying the power law $k_{cr} \sim k_C^{1/2}$, Fig. 4(a), and, for a realistic range, a decreasing function of ε following the power law $k_{cr} \sim \varepsilon^{-1/2}$, Fig. 4(b). With these three dependencies at hand, we conclude

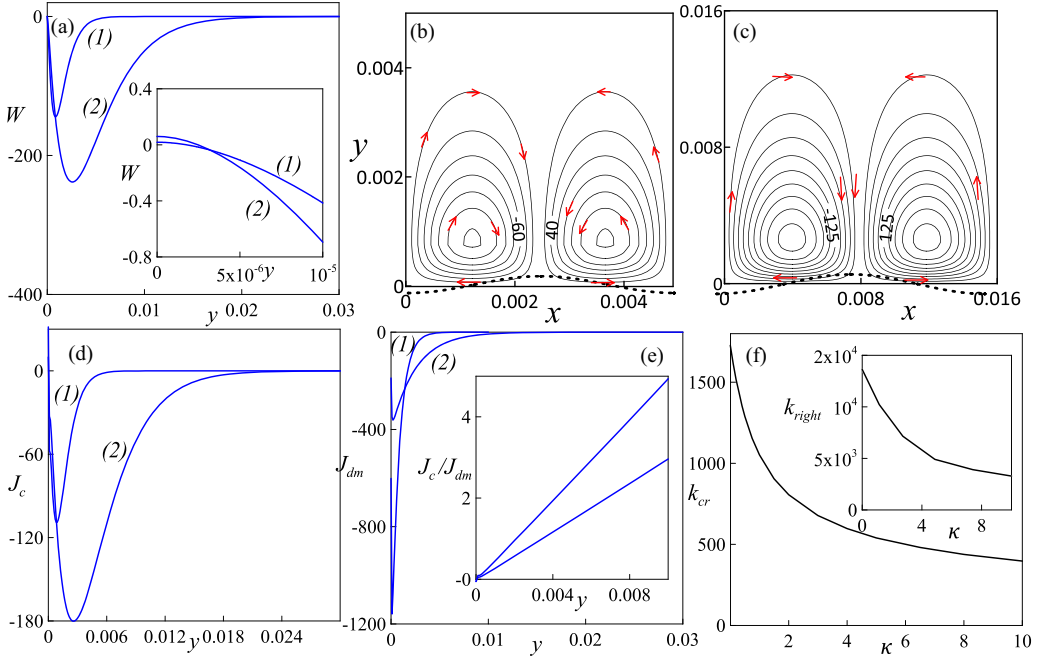


FIG. 6. (a) Vertical component of the fluid velocity, $W(y)$, vs. dimensionless distance from the electrode surface, y , for $p_1 = 10^3$, $\varepsilon = 10^{-4}$, $\lambda = 2 \times 10^{-6}$, $k_C = 10$, $V = 1$; $\kappa = 0.5$, $k = k_{cr} = 1289$ [line (1)] and $\kappa = 10$, $k = k_{cr} = 397$ [line (2)]. Inset to (a): Same plots for the vicinity of the interface; (b), (c) flow streamlines for the same parameter values: $\kappa = 0.5$, $k = k_{cr} = 1289$ (b) and $\kappa = 10$, $k = k_{cr} = 397$ (c). The dashed black line at the bottom marks the periodic electrode surface distortion. (d), (e) The dependencies of the convective flux (d) and the diffusion/migration flux (e) components on the dimensionless distance from the electrode surface for $\kappa = 0.5$, $k = k_{cr} = 1289$ [line (1)], $\kappa = 10$, $k = k_{cr} = 397$ [line (2)]; Inset to (e): the ratio of the convective and the diffusion/migration flux components vs. y ; (f) Critical wave number k_{cr} vs. κ . Inset: The dependence of the right edge, k_{right} , of the instability interval $0 \leq k \leq k_{right}$ on κ .

that the critical wave number k_{cr} is a linear function of a single parameter: $\sqrt{\frac{k_C \sqrt{p_1}}{\sqrt{2\varepsilon}}}$, Fig. 4(c). Thus, its reciprocal is the typical length in the emerging dendrite which scales as $\sqrt{\frac{\sqrt{2\varepsilon}}{k_C \sqrt{p_1}}}$ at the linear stage. In dimensional units, this yields the length scale

$$L = \sqrt{r_d \left(\frac{K_a \tilde{c}_M}{K_c c_0} \right)^{-1/2} \cdot \frac{D}{K_c}}, \quad (42)$$

which is the geometric average of the width of the highly charged portion of the EDL, typically up to 10% of the Debye length, r_d (3–10 nm), and the reaction–diffusion length, D/K_C (1 mm–10 mm). This yields L in the range of 100 nm–10 μ m, qualitatively compatible with experimental data [3,4].

We complete this part by evaluating the impact on the MI of the fluid flow generated solely by the metal surface propagation. As we show in Figs. 5(a), 5(b) for large wave numbers, MI generates two pairs of vortices. The first pair, adjacent to the interface, is dragged by the moving solid, whereas the second pair emerges due to flow continuity having the intensity proportional to surface curvature [k^2 , the second equation in (34j)]. This latter vortex pair exerts a stabilizing effect by bringing the low concentration to the propagating protrusion and the high concentration to the cavity, Fig. 5(b). However, for a dilute electrolyte, due to the slow propagation of the electrodeposition front, its induced flow velocity is too low to have a significant effect on MI. This is illustrated in

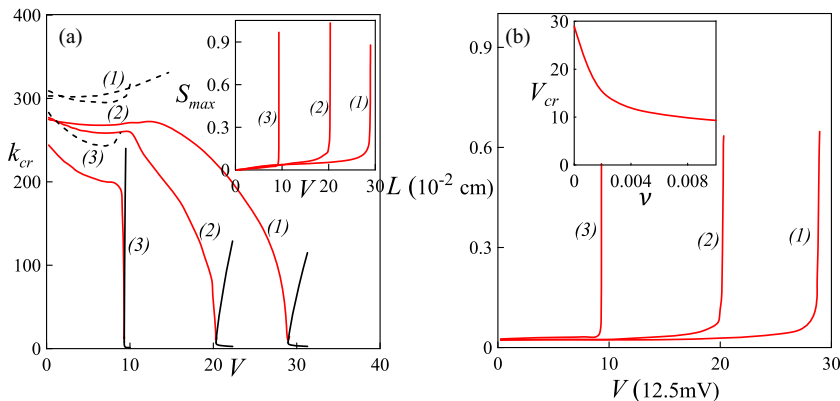


FIG. 7. (a) Red lines: critical wave number k_{cr} vs. voltage V for the set of control parameters corresponding to 100- μm wide layer of 10^{-2}M aqueous solution of copper sulfate: $p_1 = 1.4 \times 10^4$, $\varepsilon = 2 \times 10^{-5}$, $k_C = 0.02$, $\lambda = 2 \times 10^{-6}$, $\kappa = 0.15$. (1) classical pointlike-ions model $\nu = 0$, (2) intermediate steric effect, $\nu = 0.001$, corresponding to a 10 M maximum total ionic concentration for a ten-millimolar bulk solution; (3) severe steric effect, $\nu = 0.01$, corresponding to a 1 M maximum total ionic concentration for a ten-millimolar bulk solution. Dashed black lines: same dependencies for the nonelectroconvective flow case, $\kappa = 0$. Continuous black lines: neutral stability curves for the electroconvective instability alone: $z_0 = 0$. Inset: The dependence of the maximal growth rate, S_{max} , on voltage V for same values of parameters. (b) Dimensional characteristic length, $L = \frac{2\pi}{k_{cr}} \cdot l$, $l = 10^{-2}\text{ cm}$, on the dimensional applied voltage, $\tilde{V} = V \cdot \frac{RT}{2F}$. The parameters and notations are the same as for plot (a). Inset: The dependence of the electroconvective instability voltage threshold, V_{cr} , on the steric constraint parameter, ν .

Figs. 5(c), 5(d) through comparison of the linearly perturbed normal convective, $J_w = Wc_0^+$, and diffusion/migration, $J_{dm} = C^{+'} + c_0^+\Phi' + C^+\varphi_0'$, fluxes in the vicinity of the interface.

We conclude this section by addressing the effect of the electroconvective flow on the mode selection in MI. We begin with analyzing the effect of the quasiequilibrium electroosmotic flow due to nonflatness of the electrode surface produced by MI in the low-voltage regime, $J = 1$, $V \sim 2$. As we show in Fig. 6, electroosmosis dominates the fluid flow and drastically enhances the pair of secondary vortices, Figs. 6(a)–6(c). The increase of the electroconvective coupling coefficient, κ , results in enhancing the electroconvective component of flux perturbation that forms in the bulk of the EDL, Figs. 6(d), 6(e). This results in a considerable decrease of the critical wave number, k_{cr} , Fig. 6(f), and in the elimination of growth of the short-wave perturbation modes, inset to Fig. 6(f).

Next, we address the realistic values of the control parameters, see Fig. 7, corresponding to a 10^{-2} M aqueous solution of copper sulfate. We note that for the low to moderate voltage regime the decrease of the critical wave number due to the quasiequilibrium electroosmotic flow varies from few percent for an intermediate steric effect to 20% for a severe steric effect [see black dashed lines and continuous red lines in Fig. 7(a)]. A further increase of voltage induces increased depletion of the electrode/solution interface, formation of the extended space charge and its related nonequilibrium electroosmotic flow as precursors of electroosmotic instability. As shown in Fig. 7(a) with a nonequilibrium electroosmotic flow present, the critical wave number decreases by at least one order of magnitude with the increase of voltage. At the threshold voltage, for which the critical wave number attains its minimum value, the nonequilibrium electroosmotic instability occurs, see Fig. 7(a). We note that the nonflatness of the electrode surface induced by MI lowers the voltage threshold of the nonequilibrium electroosmotic instability by a few percent, compared to the flat surface case. On the other hand, the occurrence of this instability fully dominates the flow, the development of MI, and, subsequently, the growth of dendrites, Figs. 7(a), 7(b). Correspondingly, the width of the diffusion layer becomes the dominant length scale for the flow and the development of MI, Fig. 7(b). We also note a substantial effect of accounting for the finite ion size and the steric

effect on the electroconvective instability voltage threshold, inset to Fig. 7(b). This results from the EDL charge redistribution mentioned previously and the increase of the extended space charge in the steric model compared to the classical one, Fig. 2. The nonlinear stage of the nonequilibrium electroosmotic flow will be analyzed in our forthcoming paper taking into account finite ionic size.

V. CONCLUSIONS

(i) Finite cathodic reaction rate combined with a finite width of the Stern layer as an element of the fine structure of the EDL selects a finite range of wave numbers of growing perturbation modes, thus removing the short-wave catastrophe in MI. The steric correction has only a minor effect on this mode selection. The selected fastest growing mode wavelength, in the range of 100 nm–10 μ m, scales with the geometric average of the reaction-diffusion length and the Debye width of the densely charged inner part of the EDL.

(ii) The flow induced by the interface motion, as well as the equilibrium electroosmosis have only a minor effect on the wavelength selection. In contrast, the development of the nonequilibrium electroosmosis regime, related to the formation of the ESC, exerts a major effect resulting in reduction of the wave number of the fastest-growing mode by more than one order of magnitude.

(iii) For a realistically high range of FCC, taking into account the finite ionic size, yields a considerable reduction of the threshold for the nonequilibrium electroosmotic instability. Given the low overall ionic concentration in the vicinity of the concentration minimum, this is a somewhat unexpected result of the high sensitivity of this threshold to the value of the ESC.

-
- [1] W. D. Bancroft, The chemistry of electroplating, *J. Phys. Chem.* **9**, 277 (1905).
 - [2] M. Schlesinger and M. Paunovic, *Modern Electroplating* (Wiley, New York, 2010).
 - [3] L. Oniciu and L. Muresan, Some fundamental aspects of leveling and brightening of metal electrodeposition, *J. Appl. Electrochem.* **21**, 565 (1991).
 - [4] S. Shin, T. T. Al-Housseiny, B. S. Kim, H. H. Cho, and H. A. Stone, The race of nanowires: Morphological instabilities and a control strategy, *Nano Lett.* **14**, 4395 (2014).
 - [5] A. I. Hochbaum, R. Chen, R. D. Delgado, W. Liang, E. E. Garnett, M. Najarian, A. Majumdar, and P. Yang, Enhanced thermoelectric performance of rough silicon nanowires, *Nature (London)* **451**, 163 (2008).
 - [6] J. H. Han, E. Khoo, P. Bai, and M. Z. Bazant, Over-limiting current and control of dendritic growth by surface conduction in nano-pores, *Sci. Rep.* **4**, 7056 (2014).
 - [7] P. Bai, J. Li, F. R. Brushett, and M. Z. Bazant, Transition of lithium growth mechanisms in liquid electrolytes, *Energy Environ. Sci.* **9**, 3221 (2016).
 - [8] L. Frenck, G. K. Sethi, J. A. Maslyn, and N. P. Balsara, Factors that control the formation of dendrites and other morphologies on lithium metal anodes, *Front. Energy Res.* **7**, 115 (2019).
 - [9] J. Xiao, How lithium dendrites form in liquid batteries, *Science* **366**, 426 (2019).
 - [10] Z. Ning, D. S. Jolly, G. Li, R. De Meyere, S. D. Pu, Y. Chen, J. Kasemchainan, J. Ihli, Ch. Gong, B. Liu, D. L. R. Melvin, A. Bonnin, O. Magdysyuk, P. Adamson, G. O. Hartley, C. W. Monroe, T. J. Marrow, and P. G. Bruce, Visualizing plating-induced cracking in lithium-anode solid-electrolyte cells, *Nature Mater.* **20**, 1121 (2021).
 - [11] J. N. Chazalviel, Electrochemical aspects of the generation of ramified metallic electrodeposits, *Phys. Rev. A* **42**, 7355 (1990).
 - [12] V. Fleury, M. Rosso, J. N. Chazalviel, and B. Sapoval, Experimental aspects of dense morphology in copper electrodeposition, *Phys. Rev. A* **44**, 6693 (1991).
 - [13] V. Fleury, J. N. Chazalviel, and M. Rosso, Coupling of drift, diffusion, and electroconvection, in the vicinity of growing electrodeposits, *Phys. Rev. E* **48**, 1279 (1993).
 - [14] V. Fleury, J. Kaufman, and B. Hibbert, Evolution of the space-charge layer during electrochemical deposition with convection, *Phys. Rev. E* **48**, 3831 (1993).

- [15] R. Bruinsma and S. Alexander, Theory of electrohydrodynamic instabilities in electrolytic cells, *J. Chem. Phys.* **92**, 3074 (1990).
- [16] J. M. Huth, H. L. Swinney, W. D. McCormick, A. Kuhn, and F. Argoul, Role of convection in thin-layer electrodeposition, *Phys. Rev. E* **51**, 3444 (1995).
- [17] M. C. Ma, G. Li, X. Chen, L. A. Archer, and J. Wan, Suppression of dendrite growth by cross-flow in microfluidics, *Sci. Adv.* **7**, eabf6941 (2021).
- [18] G. Li, A. Townsend, L. A. Archer, and D. L. Koch, Suppression of electroconvective and morphological instabilities by an imposed cross flow of the electrolyte, *Phys. Rev. Fluids* **6**, 033701 (2021).
- [19] G. Li, A. Townsend, L. A. Archer, and D. L. Koch, Electroconvection near an ion-selective surface with Butler–Volmer kinetics, *J. Fluid Mech.* **930**, A26 (2022).
- [20] J. Elezgaray, C. Leger, and F. Argoul, Linear stability analysis of unsteady galvanostatic electrodeposition in the two-dimensional diffusion-limited regime, *J. Electrochem. Soc.* **145**, 2016 (1998).
- [21] I. Rubinstein and L. Shtilman, Voltage against current curves of cation exchange membranes, *J. Chem. Soc. Faraday Trans. II* **75**, 231 (1979).
- [22] B. M. Grafov and A. A. Chernenko, Theory of the passage of a constant current through a solution of a binary electrolyte, *Dokl. Akad. Nauk SSSR* **146**, 135 (1962).
- [23] L. Bass, Electrical structures of interfaces in steady electrolysis, *Trans. Faraday Soc.* **60**, 1656 (1964).
- [24] W. H. Smyrl and J. Newman, Double layer structure at the limiting current, *Trans. Faraday Soc.* **63**, 207 (1967).
- [25] R. P. Buck, Steady-state space-charge effects in symmetric cells with concentration polarized electrodes, *J. Electroanal. Chem.* **46**, 1 (1973).
- [26] A. V. Listovnichy, Passage of currents higher than the limiting one through the electrode-electrolyte solution system, *Sov. Electrochem.* **25**, 1651 (1989).
- [27] V. V. Nikonenko, V. I. Zabolotsky, and N. P. Gnusin, Electric transport of ions through diffusion layers with impaired electroneutrality, *Sov. Electrochem.* **25**, 262 (1989).
- [28] Y. Ben and H.-C. Chang, Nonlinear Smoluchowski slip velocity and micro-vortex generation, *J. Fluid Mech.* **461**, 229 (2002).
- [29] K. T. Chu and M. Z. Bazant, Electrochemical thin films at and above the classical limiting current, *SIAM J. Appl. Math.* **65**, 1485 (2005).
- [30] M. D. Tikekar, S. Choudhury, Z. Tu, and L. A. Archer, Design principles for electrolytes and interfaces for stable lithium-metal batteries, *Nature Energy* **1**, 16114 (2016).
- [31] M. D. Tikekar, L. A. Archer, and D. L. Koch, Stabilizing electrodeposition in elastic solid electrolytes containing immobilized anions, *Sci. Adv.* **2**, e1600320 (2016).
- [32] J. H. Han, M. Wang, P. Bai, F. R. Brushett, and M. Z. Bazant, Dendrite suppression by shock electrodeposition in charged porous media, *Sci. Rep.* **6**, 28054 (2016).
- [33] J. Zhi, Sh. Li, Mei Han, and P. Chen, Biomolecule-guided cation regulation for dendrite-free metal anodes, *Sci. Adv.* **6**, eabb1342 (2020).
- [34] E. Khoo, H. Zhao, and M. Z. Bazant, Linear stability analysis of transient electrodeposition in charged porous media: Suppression of dendritic growth by surface conduction, *J. Electrochem. Soc.* **166**, A2280 (2019).
- [35] I. Rubinstein and B. Zaltzman, The effects of reaction kinetics upon the instabilities in cathodic electrodeposition, *Curr. Opin. Colloid Interface Sci.* **60**, 101591 (2022).
- [36] C. Chen and J. Jorne, The dynamics of morphological instability during electrodeposition, *J. Electrochem. Soc.* **138**, 3305 (1991).
- [37] L. G. Sundström, and F. H. Bark, On morphological instability during electrodeposition with a stagnant binary electrolyte, *Electrochim. Acta* **40**, 599 (1995).
- [38] C. P. Nielsen and H. Bruus, Morphological instability during steady electrodeposition at overlimiting currents, *Phys. Rev. E* **92**, 052310 (2015).
- [39] I. Rubinstein and B. Zaltzman, Extended space charge in concentration polarization, *Adv. Colloid Interface Sci.* **159**, 117 (2010).
- [40] M. Wang, N.-b. Ming, and P. Bennema, Pattern formation in noise reduced electrochemical deposition, *Phys. Rev. E* **48**, 3825 (1993).

- [41] Y. F. Tu, X. H. Chao, J. P. Sang, S. Y. Huang, and X. W. Zou, Thin-layer electrode-position of Zn in the agar gel medium, *Phys. A* **387**, 4007 (2008).
- [42] P. Drude, Zur Elektronentheorie der Metalle; I. Teil, *Ann. Phys. (NY)* **306**, 566 (1900).
- [43] P. Drude, Zur Elektronentheorie der Metalle; II. Teil, Galvanomagnetische und thermomagnetische Effecte, *Ann. Phys.* **308**, 369 (1900).
- [44] P. M. Biesheuvel, M. van Soestbergen, and M. Z. Bazant, Imposed currents in galvanic cells, *Electrochim. Acta* **54**, 4857 (2009).
- [45] M. Z. Bazant, Theory of chemical kinetics and charge transfer based on nonequilibrium thermodynamics, *Acc. Chem. Res.* **46**, 1144 (2013).
- [46] I. Rubinstein, *Electrodiffusion of Ions* (SIAM, Philadelphia, 1990).
- [47] I. Rubinstein and B. Zaltzman, Electro-osmotically induced convection at a permselective membrane, *Phys. Rev. E* **62**, 2238 (2000).
- [48] B. Zaltzman and I. Rubinstein, Electro-osmotic slip and electroconvective instability, *J. Fluid Mech.* **579**, 173 (2007).
- [49] E. A. Demekhin, N. V. Nikitin, and V. S. Shelistov, Direct numerical simulation of electrokinetic instability and transition to chaotic motion, *Phys. Fluids* **25**, 122001 (2013).
- [50] E. A. Demekhin, N. V. Nikitin, and V. S. Shelistov, Three-dimensional coherent structures of electrokinetic instability, *Phys. Rev. E* **90**, 013031 (2014).
- [51] J. J. Bikerman, XXXIX. Structure and capacity of electrical double layer, *London, Edinburgh, Dublin Philos. Mag. J. Sci.* **33**, 384 (1942).
- [52] I. Borukhov, D. Andelman, and H. Orland, Steric Effects in Electrolytes: A Modified Poisson–Boltzmann Equation, *Phys. Rev. Lett.* **79**, 435 (1997).
- [53] M. S. Kilic, M. Z. Bazant, and A. Ajdari, Steric effects in the dynamics of electrolytes at large applied voltages. I. Double-layer charging, *Phys. Rev. E* **75**, 021502 (2007).
- [54] M. S. Kilic, M. Z. Bazant, and A. Ajdari, Steric effects in the dynamics of electrolytes at large applied voltages. II. Modified Poisson–Nernst–Planck equations, *Phys. Rev. E* **75**, 021503 (2007).
- [55] B. D. Storey, L. R. Edwards, M. S. Kilic, and M. Z. Bazant, Steric effects on ac electro-osmosis in dilute electrolytes, *Phys. Rev. E* **77**, 036317 (2008).
- [56] A. S. Khair and T. M. Squires, Ion steric effects on electrophoresis of a colloidal particle, *J. Fluid Mech.* **640**, 343 (2009).
- [57] M. Z. Bazant, M. S. Kilic, B. D. Storey, and A. Ajdari, Towards an understanding of induced-charge electrokinetics at large applied voltages in concentrated solutions, *Adv. Colloid Interface Sci.* **152**, 48 (2009).
- [58] M. Z. Bazant, M. S. Kilic, B. D. Storey, and A. Ajdari, Nonlinear electrokinetics at large voltages, *New J. Phys.* **11**, 075016 (2009).
- [59] M. Z. Bazant, B. D. Storey, and A. A. Kornyshev, Double Layer in Ionic Liquids: Overscreening versus Crowding, *Phys. Rev. Lett.* **106**, 046102 (2011).
- [60] B. D. Storey and M. Z. Bazant, Effects of electrostatic correlations on electrokinetic phenomena, *Phys. Rev. E* **86**, 056303 (2012).
- [61] R. F. Stout and A. S. Khair, A continuum approach to predicting electrophoretic mobility reversals, *J. Fluid Mech.* **752**, R1 (2014).
- [62] M. McEldrew, Z. A. H. Goodwin, Sh. Bi, M. Z. Bazant, and A. A. Kornyshev, Theory of ion aggregation and gelation in super-concentrated electrolytes, *J. Chem. Phys.* **152**, 234506 (2020).
- [63] Y. Avni, R. M. Adar, and D. Andelman, Charge oscillations in ionic liquids: A microscopic cluster model, *Phys. Rev. E* **101**, 010601(R) (2020).